Recent Tropical Andes Glacier Retreat Unprecedented in the Holocene

Andrew L. Gorin

A thesis

submitted to the Faculty of

the department of Earth and Environmental Science

in partial fulfillment

of the requirements for the degree of

Masters of Science

Boston College

Morrissey College of Arts and Sciences

Graduate School

August 2021

Recent Tropical Andes Glacier Retreat Unprecedented in the Holocene

Andrew L. Gorin

Advisor: Jeremy D. Shakun, PhD.

Abstract

Glaciers in the tropics have retreated over recent decades, but whether the magnitude of this retreat has exceeded the bounds of past Holocene fluctuations is unclear. In this study, we measure cosmogenic ^{10}Be and ^{14}C concentrations from recently exposed bedrock at the margin of five glaciers in the tropical Andes, including four small glaciers and the Quelccaya Ice Cap, the world's largest tropical ice mass. Concentrations at the Quelccaya Ice Cap margin suggest there was extended exposure during the first half of the Holocene, but that the site was covered by ice for the last 5 kyr. In contrast, nuclide concentrations are strikingly low in all samples at the margins of the four small glaciers, equivalent to ~200 years of ^{14}C and 50 years of ^{10}Be accumulation at surface production rates. These data suggest that the small tropical glaciers are now smaller than they have been at any point during the Holocene, whereas the Quelccaya Ice Cap has not yet retreated to its smallest extent of the Holocene, likely due to its larger size and slower response time.

Contents

List of Tables

List of Figures

Supplementary Figure S9. Synthesis of estimated global erosion rates.

Acknowledgements

I acknowledge the help and support of my many collaborators: Shaun Marcott, Brent Goehring, Andrew Jones, Tori Kennedy, Gordon Bromley, Meredith Kelly, Emilio Mateo, and Vincent Jomelli. I would also like to thank my advisor, Dr. Jeremy Shakun, for the countless hours he spent discussing this material with me, and for his contagious enthusiasm for our work. I also acknowledge funding for this work from NSF EAR-1805620 and the travel funding I received from the Boston College Graduate School of Arts and Sciences to present a portion this work at the 2019 meeting of the American Geophysical Union. Finally, I would like to thank the other two members of my thesis committee, Noah Snyder and Hilary Palevsky.

Preface

This thesis is part of an NSF-funded project to reconstruct Holocene glacier histories along the spine of the Americas led by investigators from Boston College, Tulane University, and University of Wisconsin-Madison, and involving nearly a dozen collaborators who helped sample glaciers. My M.S. research focuses on the tropical component of this project. I have written this thesis in manuscript-style in preparation for submission to Science Magazine. I will be the lead author on this forthcoming submission with the following coauthors: Jeremy Shakun, Brent Goehring, Shaun Marcott, Tori Kennedy, Andrew Jones, Gordon Bromley, Meredith Kelly, Emilio Mateo, Donald Rodbell, Bryan Mark, and Vincent Jomelli. This document is split into main text, materials and methods, and supplemental text. The submission to Science will include the main text, materials and methods, and the following subsections from the supplementary text: ^{14}C-^{10}Be Paired Chronometer, Site Descriptions, Supplementary Figures, Supplementary Tables. I processed 14 of the 25 samples presented here (and processed 38 total samples for the broader project), developed and implemented the numerical model, and led data interpretation and manuscript writing. While I did not visit the tropical sites described in this thesis, I traveled to two field sites in British Columbia and Wyoming to collect samples as part of the larger effort.

In addition to this primary manuscript, during my work as a M.S. student, I developed and implemented the numerical model used to facilitate data interpretation in Vickers et al. (2021) and Jomelli et al. (*in review*). I am a co-author on both of those studies. Those

publications explore other aspects of Holocene tropical glacier history, and include analysis of seven of the samples also discussed in the primary manuscript below.

Introduction

The global retreat of alpine glaciers is among the most visible signs of anthropogenic climate change and has accelerated over recent decades (*1*, *2*). It is unclear, however, whether this retreat has yet exceeded the natural range of fluctuations over the Holocene. Tropical glaciers may be the first place such a signal emerges because they are particularly sensitive to changes in climate (*3*) and tropical climate variability is generally small on all timescales (*4*, *5*), providing a high signal-to-noise ratio (*6*, *7*).

During the Holocene, mean annual radiative forcing in the tropics increased modestly due to orbital variations and rising greenhouse-gas concentrations (~1 W/m^2; *5*). Despite this slight increase, records from the tropical Andes and Africa generally suggest that glaciers were relatively small in the early Holocene (~12-8 ka) and subsequently grew until reaching maxima during the last millennium, similar to fluctuations in Northern Hemisphere glaciers (*8–11*) (Supplementary Text). The similar Holocene history of glaciers throughout much of the tropics suggests that they generally responded to large-scale changes in temperature. Indeed, proxy reconstructions suggest tropical temperatures generally warmed during the early Holocene and subsequently cooled from ~6 ka to present (*12*). Precipitation was more variable during the Holocene, however, increasing in the southern tropical Andes but decreasing in the northern tropical Andes due to the southward migration of the Intertropical Convergence Zone (*13–16*) and strengthening of the South American Summer Monsoon (*17*). Precipitation also decreased throughout much of East Africa as the African Humid Period ended (*18*, *19*).

To determine how small current tropical glacier extents may be in a Holocene context, we measured *in situ* ^{14}C and ^{10}Be concentrations in 25 samples of recently exposed bedrock near the margins of five alpine glaciers in the tropical Andes (Materials and Methods). The pairing of cosmogenic nuclides with different half-lives allows us to quantify the amount of time and approximately when a glacier was larger or smaller than today (Supplementary Text, Figure S1). During periods of exposure when ice is smaller, cosmic radiation produces ^{10}Be and ^{14}C in quartz near the bedrock surface, with production attenuating rapidly in the uppermost few meters of the subsurface and then continuing at low levels for tens of meters below this (*20*). Nuclide production attenuates more quickly for ^{10}Be than ^{14}C, leading to elevated $^{10}Be/^{14}C$ ratios for nuclides produced at depth, whether under rock or ice (Figure S2). During periods of burial when ice is larger, nuclide production is suppressed and nuclides decay, with the faster decay of ^{14}C ($t_{\frac{1}{2}} = 5734$ yr) than ^{10}Be ($t_{\frac{1}{2}} =$ 1.4 Myr) causing $^{14}C/^{10}Be$ ratios to decrease through time. In addition, erosion can reduce the surface concentration of both nuclides by exhuming more weakly-dosed subsurface material. Measuring multiple bedrock samples along a glacier margin can help disentangle the effects of erosion and exposure because the samples experienced the same exposure history but possibly different amounts of erosion. We assume that any pre-Holocene nuclides were removed by glaciation during the latest Pleistocene and that bedrock has only been covered by ice during the Holocene (e.g., not till).

We study Andean glaciers spanning the equator from 6°N to 16°S, subjecting them to different precipitation histories associated with past migrations of the Intertropical Convergence Zone (Figure 1). We took samples from four small glaciers (0.1 – 2.4 km^2) as well as the largest tropical ice mass in the world (Quelccaya Ice Cap, Peru, 40 km^2) (Materials and Methods, Figures S3-7). At Cocuy Glacier (6.4°N, 72.3°W, 5123 m), Zongo Glacier (16.3°S, 68.1°W, 5257 m), and the Quelccaya Ice Cap (13.9°S, 70.8°W, 5740 m), we sampled along the ice margin, while at Charquini Norte Glacier (16.3°S, 68.1°W, 5257 m) and Queshque Glacier (9.8°S, 77.3°W, 5578 m), we took samples extending from the ice margin to ~1 km downvalley. We previously reported results for the Quelccaya and downvalley Charquini Norte samples (*11*, *21*). The range of glacier sizes and sampling orientations in our study helps to constrain the extent of modern retreat for ice masses with a range of response times and recent positions in a valley. Monitoring studies indicate that most ice masses in the tropical Andes, including our glaciers, have been retreating over the past century (*22–24*) and have lost mass at an accelerated pace in recent decades (*1*). There is broad consensus that the >1°C temperature increase at high elevations in the region during the past century is sufficient to have caused this widespread glacial retreat, whereas precipitation variations have been small and spatially variable (*22–26*).

Results

Cosmogenic nuclide concentrations are strikingly low in all samples at the margins of the four small glaciers, equivalent to an average of ~200 years of ^{14}C and 50 years of ^{10}Be accumulation at surface production rates (Figure 2). Only one of these samples (Zon-5) has

an anomalously high ^{14}C concentration, but its near-zero ^{10}Be concentration suggests the elevated ^{14}C could be a result of sample contamination with atmospheric ^{14}C. Nuclide concentrations in laboratory blanks are lower than all samples, indicating that these low but non-zero sample values are robust (*20*) (Figure S8). The only exceptions to this widespread pattern of low nuclide concentrations are samples adjacent to the Quelccaya Ice Cap and two samples 0.7 km downvalley from Charquini Norte Glacier near its Little Ice Age moraine (Figure 2). These samples have ^{10}Be concentrations equivalent to several thousand years of surface exposure and $^{14}C/^{10}Be$ ratios well below the production value implying considerable decay. Modeling from our previous work suggests that these nuclide concentrations are consistent with ~5 kyr of exposure during the early Holocene followed by ~5 kyr of burial under ice cover during the late Holocene (*11*, *21*).

Discussion

The extremely low cosmogenic nuclide concentrations in recently exposed proglacial bedrock at our four small glaciers could be explained in two ways: (I) sample sites were covered by ice throughout the entirety of the Holocene preventing the buildup of nuclides, or (II) the sites experienced prior exposure but were then deeply eroded, removing most of the nuclides. We favor the former interpretation, which implies that current retreat is unprecedented in the Holocene, for several reasons.

All samples with low cosmogenic nuclide concentrations have elevated $^{14}C/^{10}Be$ ratios (~1.5 to 9 times the production ratio), which is consistent with low-level production through ice due to the less rapid attenuation of ^{14}C production with depth than ^{10}Be.

Modeling confirms this expectation of low concentrations and high $^{14}C/^{10}Be$ ratios under persistent ice cover, though it does not allow for ratios as high as we measured for realistic ice thicknesses (several tens of meters) (Materials and Methods, Figure 3). This discrepancy may reflect uncertainties in the attenuation length of ^{14}C production, which is poorly constrained (*27*).

The higher nuclide concentrations in samples near the Charquini Norte Glacier Little Ice moraine and the margin of the Quelccaya Ice Cap are also consistent with tropical glaciers currently retreating to their smallest extent of the Holocene. The downvalley Charquini samples were apparently exposed earlier in the Holocene prior to the Little Ice Age maximum, but the low nuclide concentrations in samples at the modern glacier front imply that they were never exposed until recent retreat shifted the ice margin far up valley. While this result is not seen in the farthest downvalley samples from Queshque glacier (i.e., they contain few nuclides), the Queshque valley is less steep than the Charquini valley, implying that the magnitude of its retreat might be larger for a given rise in equilibrium line altitude. In a similar manner, the retreat of the Quelccaya Ice Cap is plausibly lagging behind the other glaciers in our study due to its larger size and likely slower response time. Therefore, we suggest that Quelccaya is also retreating toward its smallest extent of the Holocene, but has not yet had enough time to reach this extent. In addition, the Quelccaya samples were collected in 2003 and 2008 (Table S1) and thus not positioned to detect the most recent retreat of the ice cap.

The spatial ubiquity of low nuclide concentrations in ice marginal bedrock spanning the tropical Andes further supports larger ice extents throughout the Holocene to explain this signal rather than deep erosion. Whereas coherent glacier extent histories are readily attributable to large-scale changes in climate, erosion rates likely exhibit greater spatial variability (*28*). Moreover, erosion is likely especially localized when associated with glacial plucking, which is typically needed to explain high erosion rates (*29*).

To consider the viability of erosion removing nuclides from early Holocene exposure, we modeled the ^{10}Be and ^{14}C concentrations that result from a plausible tropical ice extent history of 5 kyr of exposure followed by 5 kyr of burial (*8*, *11*, *21*) under a range of subglacial erosion rates and ice thicknesses (*20*). These calculations show that glacial erosion rates would have to exceed 0.5 mm/yr to reduce nuclide concentrations from early Holocene exposure to values congruous with our measurements (Figure 4). Syntheses of alpine subglacial erosion rates suggest erosion rates this high sustained for millennia are unlikely for the tropical glaciers we examined (*20*) (Figure S9). While subglacial erosion rates vary from 0.01-1000 mm/yr, the highest estimates of subglacial erosion rates, ~100-1000 mm/yr, are from Alaskan and Patagonian glaciers, where large and rapidly fluctuating amounts of meltwater promote efficient sediment evacuation and subglacial plucking (*28*). Koppes et al. (*28*) found that glaciers in climates with a mean annual temperature below 0°C, such as those in our study, typically erode ~0.01-0.1 mm/yr. Furthermore, erosion rate estimates also have a timescale bias, with shorter timescales producing higher apparent erosion rates than longer timescales (*30*). Finally, some of our tropical glaciers, including

Charquini Norte and Cocuy Glacier, lack the substantial ice thickness needed to erode at these fastest rates (*28*).

Our previous work modeling the higher cosmogenic nuclide concentrations downvalley from Charquini Norte and adjacent to Quelccaya, as well as at a site that deglaciated in the mid-20th century in the Rwenzori Mountains of Uganda, also supports Holocene erosion rates ≤ 0.5 mm/yr, with most estimates between 0.01-0.25 mm/yr (*11*, *21*). Indeed, the substantial nuclide concentrations in those tropical samples imply that late Holocene erosion was insufficient to remove most nuclides produced during early Holocene exposure. These rates also agree with estimates based on Holocene clastic sediment fluxes to proglacial lakes in the tropical Andes (*8*), which suggest erosion rates of 0.01-0.1 mm/yr (*20*) (Materials and Methods, Table S5). Finally, the low volumes of till and lack of stepped topography at our samples sites do not support the high rates of sediment generation or bedrock plucking that would be required to strip off the top few meters of material irradiated by early Holocene exposure.

While these arguments collectively suggest that the low cosmogenic nuclide concentrations in most of our proglacial bedrock samples reflect continuous ice cover throughout the Holocene, it would have important implications for landscape evolution if they are instead attributable to deep erosion during recent millennia. The implied glacial erosion rates would yield at least 1.25 km of erosion if extended over the Pleistocene, or likely more considering that these glaciers were larger and likely more erosive during glacial periods. Temporally sustained values this high would considerably exceed estimated rates of

Andean uplift during the same period of 0.2-0.3 mm/yr, and suggest glacial erosion is lowering the Andes, inconsistent with observations (*31*).

Conclusion

Our results indicate that several tropical Andean glaciers have now exceeded the range of their Holocene length variations and are smaller than they have been at any time during the current interglacial. The consistency of this result between sites spanning ~22° of latitude suggests that rising temperatures and not changing precipitation patterns are responsible for this unprecedented glacial retreat, as precipitation-driven glacier extent changes were likely spatially variable during the Holocene. This inference is in agreement with a recent compilation of Holocene paleoclimate reconstructions, which suggests tropical temperatures have recently surpassed their Holocene maximum (*12*). Since tropical glaciers are particularly sensitive indicators of climate change, this finding reflects the profound changes already materializing in the region, which may not yet be visible in other climate indicators or regions. The departure of tropical climate from its interglacial range has important implications for a biosphere adapted to a limited range of conditions as well as the future of freshwater availability in the Andes where as much as 50% of drinking water originates from glacial ice (*32*).

Figures

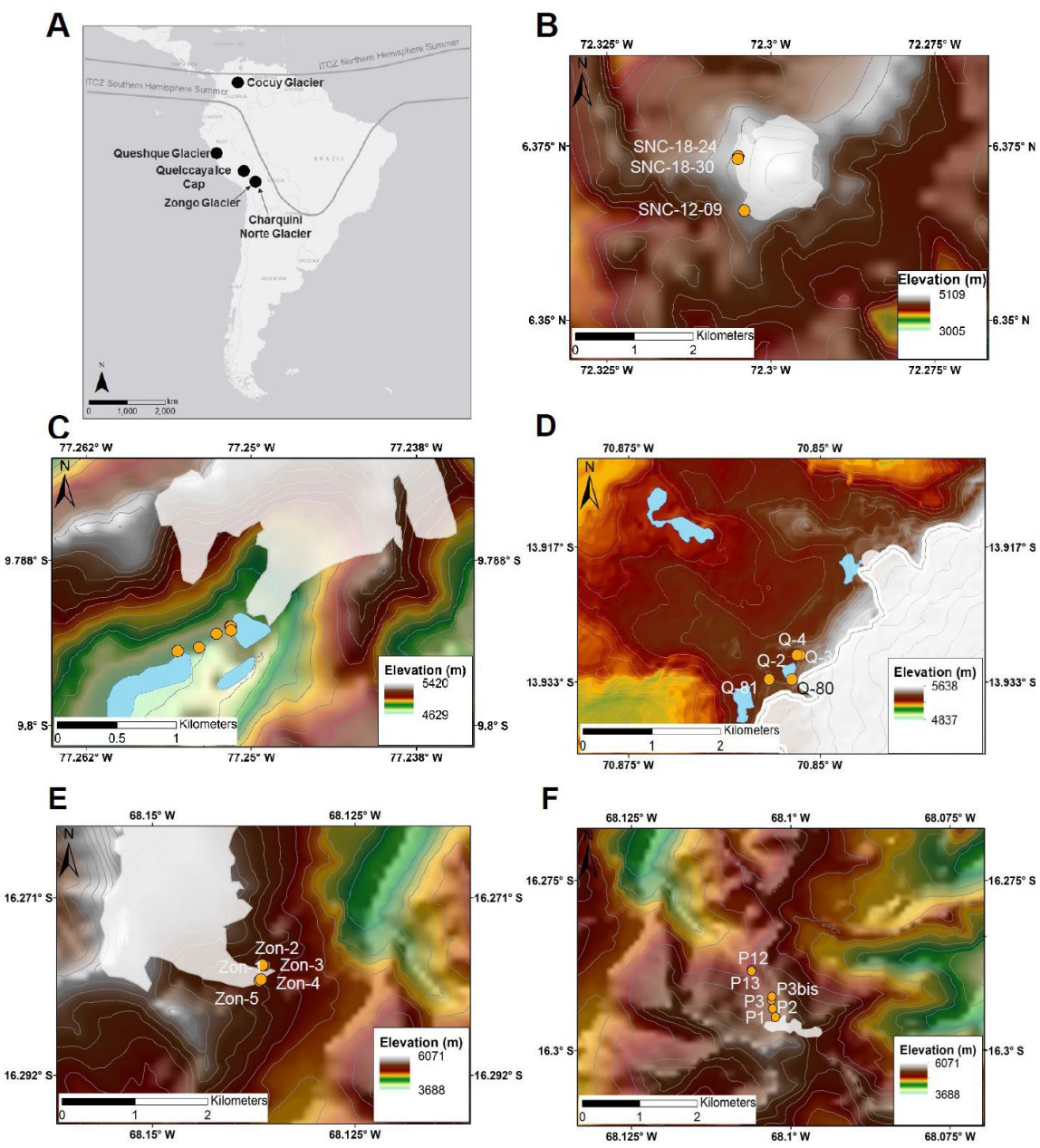
A
ITCZ Northern Hemisphere Summer
ITCZ Southern Hemisphere Summer
Cocuy Glacier
Queshque Glacier
Quelccaya Ice Cap
Zongo Glacier
Charquini Norte Glacier
B
SNC-18-24
SNC-18-30
SNC-12-09
Elevation (m)
5109
3005
Kilometers
C
Elevation (m)
5420
4629
Kilometers
D
Q-4
Q-2
Q-3
Q-81
Q-80
Elevation (m)
5638
4837
Kilometers
E
Zon-2
Zon-3
Zon-4
Zon-5
Elevation (m)
6071
3688
Kilometers
F
P12
P13
P3bis
P3
P2
P1
Elevation (m)
6071
3688
Kilometers

Figure 1: Glaciers studied in this project. A: Locations of glaciers in South America. B-F: Maps of B: Cocuy Glacier, C: Queshque Glacier, D: Quelccaya Ice Cap, E: Zongo Glacier, F: Charquini Norte Glacier. Orange circles indicate sample locations and white regions represent current glacier extents in panels in B-F.

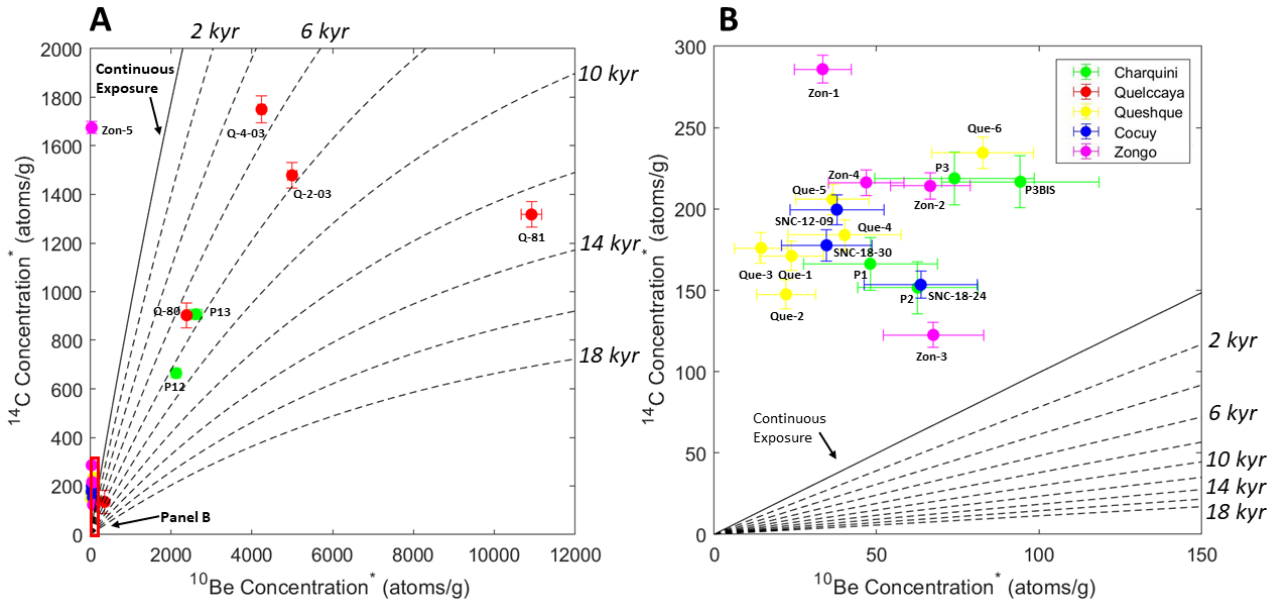

Figure 2: A: ^{14}C and ^{10}Be concentrations with 1σ uncertainties from all samples analyzed in this study. Nuclide concentrations are normalized by their local surface production rate such that ^{10}Be concentrations are equivalent to years of surface production. Solid black line shows evolution of surface concentrations with continuous exposure. Dotted lines show burial isochrones. The plot does not consider erosion. B: Zoomed in plot of the low-nuclide concentration samples. They all plot above the continuous surface exposure curve, indicating production at depth.

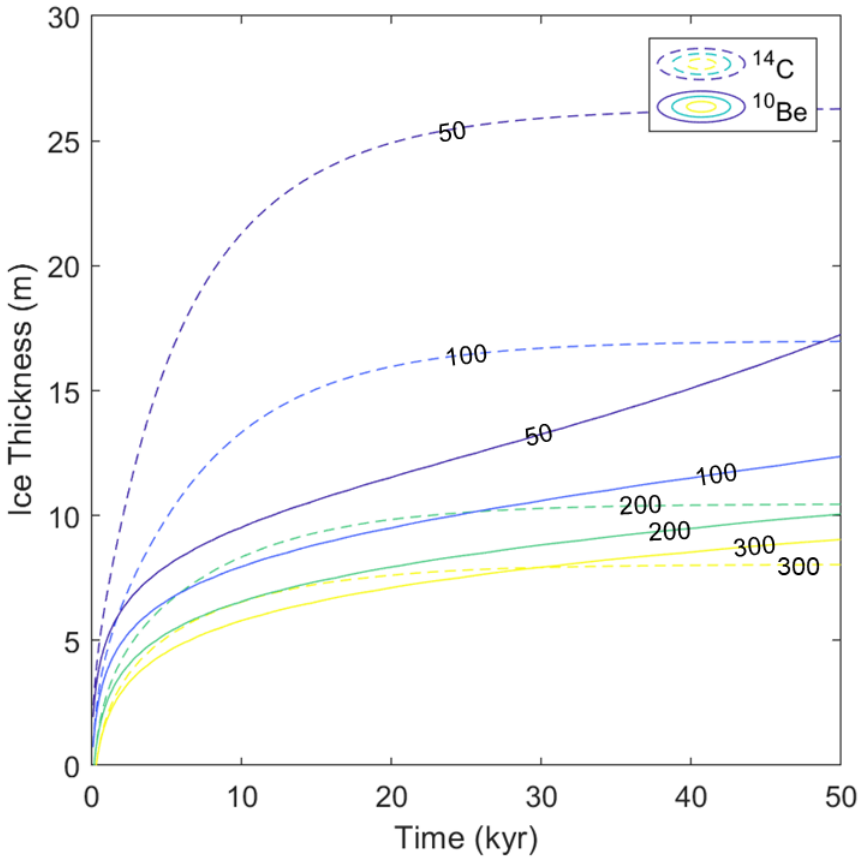

Figure 3: Modeled ^{10}Be and ^{14}C accumulation in a bedrock surface through glacial ice over 50 kyr. Nuclide concentrations are normalized by the surface production rate and are thus equivalent to years of surface exposure. Dashed lines represent ^{14}C and solid lines represent ^{10}Be. Under realistic ice thicknesses of ≥ 20 m we expect only ~50 years' worth of ^{14}C and <50 years' worth of ^{10}Be. These somewhat lower estimates compared to our measurements may be explained by uncertainties in the attenuation of nuclide production with depth (27).

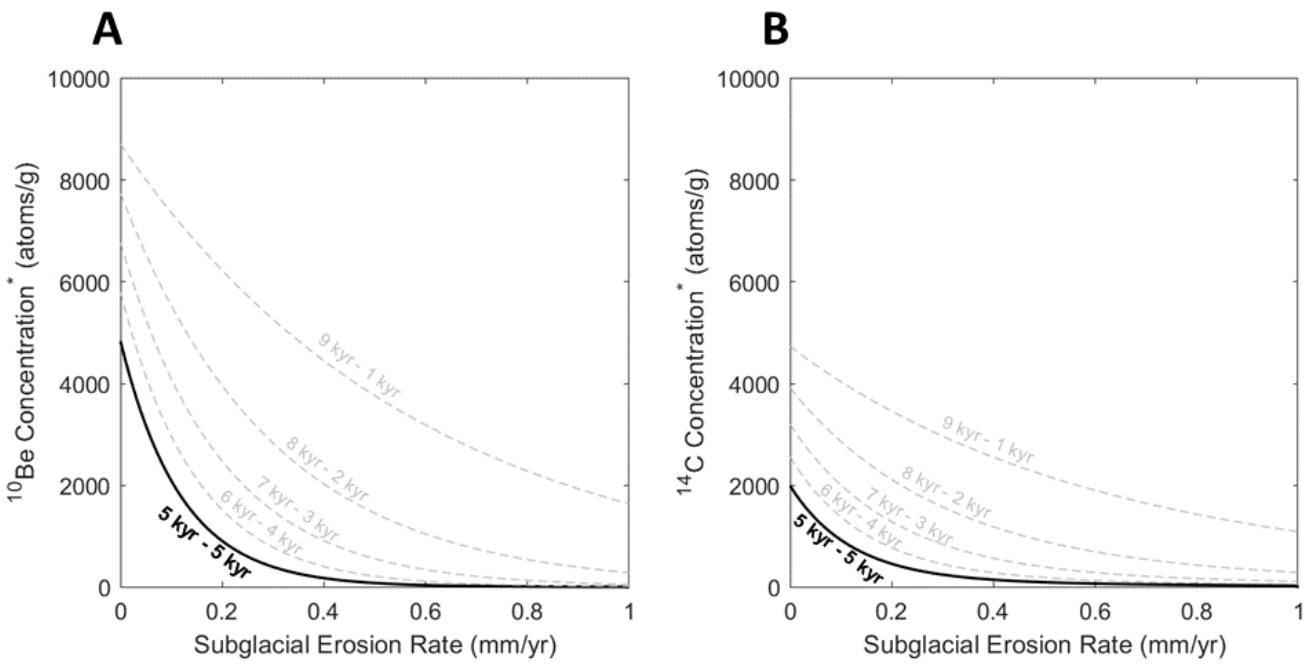

Figure 4: A: Modeled ^{10}Be concentrations resulting from five Holocene exposure-burial histories for various subglacial erosion rates; 5 kyr – 5kyr indicates 5 kyr of exposure followed by 5 kyr of burial and is bolded because it is considered the most likely history. Calculations do not include nuclide production through ice during burial or erosion during exposure. B: Same as panel A but for ^{14}C. Nuclide concentrations are normalized by the surface production rate.

References

1. R. Hugonnet, R. McNabb, E. Berthier, B. Menounos, C. Nuth, L. Girod, D. Farinotti, M. Huss, I. Dussaillant, F. Brun, A. Kääb, Accelerated global glacier mass loss in the early twenty-first century. *Nature*. **592**, 726–731 (2021).

2. B. Marzeion, J. G. Cogley, K. Richter, D. Parkes, Attribution of global glacier mass loss to anthropogenic and natural causes. *Science*. **345**, 919–921 (2014).

3. S. Hastenrath, Climatic forcing of glacier thinning on the mountains of equatorial East Africa. *Int. J. Climatol.* **30**, 146–152 (2010).

4. P. Huybers, W. Curry, Links between annual, Milankovitch and continuum temperature variability. *Nature*. **441**, 329–332 (2006).

5. H. Wanner, L. Mercolli, M. Grosjean, S. P. Ritz, Holocene climate variability and change; a data-based review. *J. Geol. Soc.* **172**, 254–263 (2015).

6. C. Mora, A. G. Frazier, R. J. Longman, R. S. Dacks, M. M. Walton, E. J. Tong, J. J. Sanchez, L. R. Kaiser, Y. O. Stender, J. M. Anderson, C. M. Ambrosino, I. Fernandez-Silva, L. M. Giuseffi, T. W. Giambelluca, The projected timing of climate departure from recent variability. *Nature*. **502**, 183–187 (2013).

7. G. H. Roe, M. B. Baker, F. Herla, Centennial glacier retreat as categorical evidence of regional climate change. *Nat. Geosci.* **10**, 95–99 (2017).

8. D. T. Rodbell, G. O. Seltzer, B. G. Mark, J. A. Smith, M. B. Abbott, Clastic sediment flux to tropical Andean lakes: records of glaciation and soil erosion. *Quat. Sci. Rev.* **27**, 1612–1626 (2008).

9. A. M. Buffen, L. G. Thompson, E. Mosley-Thompson, K. I. Huh, Recently exposed vegetation reveals Holocene changes in the extent of the Quelccaya Ice Cap, Peru. *Quat. Res.* **72**, 157–163 (2009).

10. O. N. Solomina, R. S. Bradley, D. A. Hodgson, S. Ivy-Ochs, V. Jomelli, A. N. Mackintosh, A. Nesje, L. A. Owen, H. Wanner, G. C. Wiles, N. E. Young, Holocene glacier fluctuations. *Quat. Sci. Rev.* **111**, 9–34 (2015).

11. A. C. Vickers, J. D. Shakun, B. M. Goehring, A. Gorin, M. A. Kelly, M. S. Jackson, A. Doughty, J. Russell, Similar Holocene glaciation histories in tropical South America and Africa. *Geology*. **49**, 140–144 (2021).

12. D. Kaufman, N. McKay, C. Routson, M. Erb, C. Dätwyler, P. S. Sommer, O. Heiri, B. Davis, Holocene global mean surface temperature, a multi-method reconstruction approach. *Sci. Data*. **7**, 201 (2020).

13. G. Seltzer, D. Rodbell, S. Burns, Isotopic evidence for late Quaternary climatic change in tropical South America. *Geology*. **28**, 35–38 (2000).

14. G. H. Haug, Southward Migration of the Intertropical Convergence Zone Through the Holocene. *Science*. **293**, 1304–1308 (2001).

15. V. Rull, M. B. Abbott, P. J. Polissar, A. P. Wolfe, M. Bezada, R. S. Bradley, 15,000-yr Pollen Record of Vegetation change in the High Altitude Tropical Andes at Laguna Verde Alta, Venezuela. *Quat. Res.* **64**, 308–317 (2005).

16. N. D. Stansell, D. T. Rodbell, M. B. Abbott, B. G. Mark, Proglacial lake sediment records of Holocene climate change in the western Cordillera of Peru. *Quat. Sci. Rev.* **70**, 1–14 (2013).

17. L. C. Kanner, S. J. Burns, H. Cheng, R. L. Edwards, M. Vuille, High-resolution variability of the South American summer monsoon over the last seven millennia: insights from a speleothem record from the central Peruvian Andes. *Quat. Sci. Rev.* **75**, 1–10 (2013).

18. F. Gasse, Hydrological changes in the African tropics since the Last Glacial Maximum. *Quat. Sci. Rev.* **19**, 189–211 (2000).

19. T. M. Shanahan, N. P. McKay, K. A. Hughen, J. T. Overpeck, B. Otto-Bliesner, C. W. Heil, J. King, C. A. Scholz, J. Peck, The time-transgressive termination of the African Humid Period. *Nat. Geosci.* **8**, 140–144 (2015).

20. Materials and methods are available as supplementary materials at the Science website.

21. V. Jomelli, D. Swingedouw, Mathias. Vuille, V. Favier, B. M. Goehring, J. D. Shakun, R. Braucher, I. Schimmelpfennig, L. Menviel, A. Rabatel, L. C. P. Martin, C. P.-H., M. Lupker, M. Christl, Z. He, D. Verfaillie, A. Gorin, G. Aumaitre, D. L. Bourles, K.

Keddadouche, AMOC control on Holocene glacier changes in the Tropical Andes and North Atlantic Region. *Rev.* (2021).

22. B. G. Mark, G. O. Seltzer, Evaluation of recent glacier recession in the Cordillera Blanca, Peru (AD 1962–1999): spatial distribution of mass loss and climatic forcing. *Quat. Sci. Rev.* **24**, 2265–2280 (2005).

23. M. Vuille, B. Francou, P. Wagnon, I. Juen, G. Kaser, B. G. Mark, R. S. Bradley, Climate change and tropical Andean glaciers: Past, present and future. *Earth-Sci. Rev.* **89**, 79–96 (2008).

24. J. L. Ceballos, C. Euscátegui, J. Ramírez, M. Cañon, C. Huggel, W. Haeberli, H. Machguth, Fast shrinkage of tropical glaciers in Colombia. *Ann. Glaciol.* **43**, 194–201 (2006).

25. G. Poveda, K. Pineda, Reassessment of Colombia's tropical glaciers retreat rates: are they bound to disappear during the 2010–2020 decade? *Adv. Geosci.* **22**, 107–116 (2009).

26. N. D. Stansell, J. M. Licciardi, D. T. Rodbell, B. G. Mark, Tropical ocean-atmospheric forcing of Late Glacial and Holocene glacier fluctuations in the Cordillera Blanca, Peru. *Geophys. Res. Lett.* **44**, 4176–4185 (2017).

27. F. M. Phillips, D. C. Argento, G. Balco, M. W. Caffee, J. Clem, T. J. Dunai, R. Finkel, B. Goehring, J. C. Gosse, A. M. Hudson, A. J. T. Jull, M. A. Kelly, M. Kurz, D. Lal, N. Lifton, S. M. Marrero, K. Nishiizumi, R. C. Reedy, J. Schaefer, J. O. H. Stone, T.

Swanson, M. G. Zreda, The CRONUS-Earth Project: A synthesis. *Quat. Geochronol.* **31**, 119–154 (2016).

28. M. Koppes, B. Hallet, E. Rignot, J. Mouginot, J. S. Wellner, K. Boldt, Observed latitudinal variations in erosion as a function of glacier dynamics. *Nature*. **526**, 100–103 (2015).

29. B. Hallet, Glacial quarrying: a simple theoretical model. *Ann. Glaciol.* **22**, 1–8 (1996).

30. V. Ganti, C. von Hagke, D. Scherler, M. P. Lamb, W. W. Fischer, J.-P. Avouac, Time scale bias in erosion rates of glaciated landscapes. *Sci. Adv.* **2**, e1600204 (2016).

31. K. M. Gregory-Wodzicki, Uplift history of the Central and Northern Andes: A review. *GSA Bull.* **112**, 1091–1105 (2000).

32. W. Vergara, A. Deeb, A. Valencia, R. Bradley, B. Francou, A. Zarzar, A. Grünwaldt, S. Haeussling, Economic impacts of rapid glacier retreat in the Andes. *Eos Trans. Am. Geophys. Union*. **88**, 261–264 (2007).

33. L. B. Corbett, P. R. Bierman, D. H. Rood, An approach for optimizing in situ cosmogenic 10Be sample preparation. *Quat. Geochronol.* **33**, 24–34 (2016).

34. A. L. Hunt, J. Larsen, P. R. Bierman, G. A. Petrucci, Investigation of Factors That Affect the Sensitivity of Accelerator Mass Spectrometry for Cosmogenic ^{10}Be and ^{26}Al Isotope Analysis. *Anal. Chem.* **80**, 1656–1663 (2008).

35. N. A. Lifton, A. J. T. Jull, J. Quade, A new extraction technique and production rate estimate for in situ cosmogenic 14C in quartz. *Geochim. Cosmochim. Acta*. **65**, 1953–1969 (2001).

36. B. M. Goehring, J. Wilson, K. Nichols, A fully automated system for the extraction of in situ cosmogenic carbon-14 in the Tulane University cosmogenic nuclide laboratory. *Nucl. Instrum. Methods Phys. Res. Sect. B Beam Interact. Mater. At.* **455**, 284–292 (2019).

37. P. Muzikar, B. Goehring, N. Lifton, Handling Overdispersion in CRONUS-Earth Intercomparison Measurements: A Bayesian Approach. *Radiocarbon*. **59**, 1133–1145 (2017).

38. K. Cuffey, W. S. B. Paterson, *The physics of glaciers* (Butterworth-Heinemann/Elsevier, Burlington, MA, 4th ed., 2010).

39. G. Balco, J. O. Stone, N. A. Lifton, T. J. Dunai, A complete and easily accessible means of calculating surface exposure ages or erosion rates from 10Be and 26Al measurements. *Quat. Geochronol.* **3**, 174–195 (2008).

40. N. Lifton, T. Sato, T. J. Dunai, Scaling in situ cosmogenic nuclide production rates using analytical approximations to atmospheric cosmic-ray fluxes. *Earth Planet. Sci. Lett.* **386**, 149–160 (2014).

41. G. Balco, Contributions and unrealized potential contributions of cosmogenic-nuclide exposure dating to glacier chronology, 1990–2010. *Quat. Sci. Rev.* **30**, 3–27 (2011).

42. J. C. Gosse, F. M. Phillips, Terrestrial in situ cosmogenic nuclides: theory and application. *Quat. Sci. Rev.* **20**, 1475–1560 (2001).

43. B. Borchers, S. Marrero, G. Balco, M. Caffee, B. Goehring, N. Lifton, K. Nishiizumi, F. Phillips, J. Schaefer, J. Stone, Geological calibration of spallation production rates in the CRONUS-Earth project. *Quat. Geochronol.* **31**, 188–198 (2016).

44. B. M. Goehring, P. Muzikar, N. A. Lifton, An in situ 14C–10Be Bayesian isochron approach for interpreting complex glacial histories. *Quat. Geochronol.* **15**, 61–66 (2013).

45. K. Hippe, Constraining processes of landscape change with combined in situ cosmogenic 14C-10Be analysis. *Quat. Sci. Rev.* **173**, 1–19 (2017).

46. G. Kaser, H. Osmaston, H. A. Osmaston, *Tropical glaciers* (Cambridge Univ. Press, Cambridge, Digitally printed first paperback version (with corr.)., 2006), *International hydrology series*.

47. R. D. Garreaud, M. Vuille, R. Compagnucci, J. Marengo, Present-day South American climate. *Palaeogeogr. Palaeoclimatol. Palaeoecol.* **281**, 180–195 (2009).

48. W. S. Lavado Casimiro, D. Labat, J. Ronchail, J. C. Espinoza, J. L. Guyot, *Hydrol. Process.*, in press, doi:10.1002/hyp.9418.

49. S, Viviane B, *The South American Monsoon System Climatology and Variability* (2012; https://openresearchlibrary.org/content/8ec361d3-ccfc-4641-b044-2c565c64d5b4).

50. E. A. Sagredo, S. Rupper, T. V. Lowell, Sensitivities of the equilibrium line altitude to temperature and precipitation changes along the Andes. *Quat. Res.* **81**, 355–366 (2014).

51. T. Van Der Hammen, J. Barelds, H. De Jong, A. A. De Veer, Glacial sequence and environmental history in the Sierra Nevada del cocuy (Colombia). *Palaeogeogr. Palaeoclimatol. Palaeoecol.* **32**, 247–340 (1980).

52. N. D. Stansell, P. J. Polissar, M. B. Abbott, M. Bezada, B. A. Steinman, C. Braun, Proglacial lake sediment records reveal Holocene climate changes in the Venezuelan Andes. *Quat. Sci. Rev.* **89**, 44–55 (2014).

53. K. Huh, M. Baraër, B. Mark, Y. Ahn, Evaluating Glacier Volume Changes since the Little Ice Age Maximum and Consequences for Stream Flow by Integrating Models of Glacier Flow and Hydrology in the Cordillera Blanca, Peruvian Andes. *Water*. **10**, 1732 (2018).

54. M. Vuille, R. S. Bradley, M. Werner, F. Keimig, 20th Century Climate Change in the Tropical Andes: Observations and Model Results. *Clim. Change*. **59**, 75–99 (2003).

55. A. Rabatel, A. Machaca, B. Francou, V. Jomelli, Glacier recession on Cerro Charquini (16° S), Bolivia, since the maximum of the Little Ice Age (17th century). *J. Glaciol.* **52**, 110–118 (2006).

56. G. O. Seltzer, D. T. Rodbell, M. Abbott, Andean glacial lakes and climate variability since the last glacial maximum. *Bull. L'institut Francais D'Etudes Andin.* **24**, 539–549 (1995).

57. J. A. Smith, Early Local Last Glacial Maximum in the Tropical Andes. *Science*. **308**, 678–681 (2005).

58. G. O. Seltzer, Late Quaternary glaciation of the Cordillera Real, Bolivia. *J. Quat. Sci.* **7**, 87–98 (1992).

59. D. T. Rodbell, J. A. Smith, B. G. Mark, Glaciation in the Andes during the Lateglacial and Holocene. *Quat. Sci. Rev.* **28**, 2165–2212 (2009).

60. M. N. Hanshaw, B. Bookhagen, Glacial areas, lake areas, and snow lines from 1975 to 2012: status of the Cordillera Vilcanota, including the Quelccaya Ice Cap, northern central Andes, Peru. *The Cryosphere*. **8**, 359–376 (2014).

61. C. Seiler, R. W. A. Hutjes, P. Kabat, Climate Variability and Trends in Bolivia. *J. Appl. Meteorol. Climatol.* **52**, 130–146 (2013).

62. H. Heidinger, L. Carvalho, C. Jones, A. Posadas, R. Quiroz, A new assessment in total and extreme rainfall trends over central and southern Peruvian Andes during 1965-2010: Rainfall Trends Over Central and Southern Peruvian Andes. *Int. J. Climatol.* **38**, e998–e1015 (2018).

63. A. Rabatel, B. Francou, A. Soruco, J. Gomez, B. Cáceres, J. L. Ceballos, R. Basantes, M. Vuille, J.-E. Sicart, C. Huggel, M. Scheel, Y. Lejeune, Y. Arnaud, M. Collet, T. Condom, G. Consoli, V. Favier, V. Jomelli, R. Galarraga, P. Ginot, L. Maisincho, J. Mendoza, M. Ménégoz, E. Ramirez, P. Ribstein, W. Suarez, M. Villacis, P. Wagnon,

Current state of glaciers in the tropical Andes: a multi-century perspective on glacier evolution and climate change. *The Cryosphere*. **7**, 81–102 (2013).

64. M. A. Kelly, T. V. Lowell, P. J. Applegate, C. A. Smith, F. M. Phillips, A. M. Hudson, Late glacial fluctuations of Quelccaya Ice Cap, southeastern Peru. *Geology*. **40**, 991–994 (2012).

65. J. S. Stroup, M. A. Kelly, T. V. Lowell, P. J. Applegate, J. A. Howley, Late Holocene fluctuations of Qori Kalis outlet glacier, Quelccaya Ice Cap, Peruvian Andes. *Geology*. **42**, 347–350 (2014).

66. M. N. Koppes, D. R. Montgomery, The relative efficacy of fluvial and glacial erosion over modern to orogenic timescales. *Nat. Geosci.* **2**, 644–647 (2009).

Materials and Methods

Field Methods

Collaborators familiar with their respective field sites sampled bedrock at the current toe of the five glaciers we studied, as well as extending 1 km downvalley at two of the sites (Table S1). Samples at each location were selected carefully to find bedrock that had experienced the same exposure-burial history, but varying quantities of erosion, which helps to unravel their effects. To find such samples, we chose rock along the current ice margin, which improves our chances of finding surfaces that experienced the same exposure-burial history. We also sampled bedrock in front of both the sides and center of the glacier, increasing the likelihood of finding surfaces that experienced variable amounts of erosion.

After selecting sample locations, chunks of bedrock were manually extracted with a hammer and chisel, and topographic shielding was estimated with an inclinometer. Samples from local high points were favored because this minimizes the chance that they were deeply eroded or buried under till for extended periods of time.

Sample Processing and Measurement

Bedrock samples were reduced to pure quartz by a series of increasingly aggressive techniques at Boston College. Whole-rock samples were first crushed to reduce them to sand, or individual mineral grain size. Magnetic minerals were then removed using a Frantz

magnetic separator. Feldspathic mineral grains and micas were subsequently removed by suspending the remaining fraction in a frothed flotation solution consisting of carbonated water, acetic acid, and laurel amine. This technique separates mineral grains by their ability to float and exploits the tendency of quartz to sink in such a solution. Finally, a series of HNO_3-HF etches dissolved remaining minerals and removed meteoric ^{10}Be from the quartz (*33*). About 20 g of quartz was used for ^{10}Be analysis whenever possible and 5 g of quartz for ^{14}C analysis.

Next, beryllium was extracted from the quartz through an extensive chemical process at one of three laboratories. Quelccaya Ice Cap samples were processed at Dartmouth College, Charquini Norte Glacier samples were processed at Tulane University, and Queshque Glacier, Cocuy Glacier, and Zongo Glacier samples were processed at the University of Wisconsin, Madison. The quartz was dissolved in HF, after which the remaining fluorides were volatilized by perchloric and hydrochloric acids and then allowed to evaporate completely. Each sample was next spiked with a known quantity of ^{9}Be and column chemistry was used to separate beryllium from the other chemical components (*33*, *34*). Finally, the pure beryllium was burned in an incinerator to oxidize it, yielding BeO^-. Sample $^{10}Be/^{9}Be$ ratios were measured by AMS at the Purdue Rare Isotope Measurement Laboratory, and converted to ^{10}Be concentrations using the known quantity of ^{9}Be from the spike (Table S2). One or two process blanks were run with each batch depending on the size of the batch.

Historically, the natural ubiquity of atmospheric ^{14}C made quartz ^{14}C isolation difficult (*35*). We extracted ^{14}C using the newly developed and primarily automated process outlined by Goehring et al. (*36*) at Tulane University. Samples were first heated to 500°C in a resistance furnace, removing atmospheric ^{14}C. Subsequent heating to 850 °C released the in situ quartz ^{14}C as CO, which reacted with $LiBO_2$ to produce CO_2. This final product was distilled into graphite-form and measured via AMS at the National Ocean Sciences Accelerator Mass Spectrometer at Woods Hole Oceanographic Institution (Table S3).

Blank Corrections

Interpretation of cosmogenic nuclide concentrations as low as those measured in this study requires careful correction with laboratory blanks. Measured sample ^{10}Be was corrected with either the average and standard deviation of the process blanks measured during each batch (for batches with multiple blanks), or the measured blank value and uncertainty (for batches with only one blank). Samples with low nuclide concentrations had ^{10}Be blanks that represented no more than 40% of the total nuclide concentration of the sample (Figure S8, Table S4). The low but detectable ^{10}Be signal among the low-nuclide samples appears robust as it was measured in samples processed by three different labs.

^{14}C samples were corrected with a long-term statistical characterization of the average and standard deviation of blank measurements from April 2019 until the time each sample was processed using the Press Method (Table S1, *35*).

Monte Carlo Forward Model

We developed a numerical model to simulate nuclide production, decay, erosion, and ice of varying thicknesses to test possible glacier histories that yield cosmogenic nuclide concentrations and ratios in agreement with the measured values for each sample (*11*). The model simulates a bedrock depth profile of ^{10}Be and ^{14}C concentrations through time for various, pre-prescribed exposure scenarios, driving production when exposed, and decay and erosion when ice covered. During periods of burial, we choose an ice thickness, and calculate the production rate at depth below this amount of ice by assuming a constant ice density of 0.917 g/cm^3 (*38*). Production during exposure and decay rates are fixed, but erosion rates and ice thicknesses are systematically adjusted to explore a range of possibilities for each exposure scenario. Production rate profiles are derived from the University of Washington online cosmogenic calculator v3 (*39*) using the LSDn scaling scheme (*40*) with the global production rate calibration dataset. The evolution of nuclide concentrations in a bedrock column are then driven by a prescribed exposure/erosion scenario in 100-year time steps via equation 1.

$$N(z,t) = P_{NT}(z) + N(Z,t-1) * e^{-\lambda_N t} \quad (1)$$

Where N is the concentration of the nuclide in the bedrock as a function of depth (z) and time (t), P_{NT} is the total production of the nuclide via spallation and muon production as a function of depth, and λN is the decay constant of the nuclide. During times of exposure, the model uses the production portion of equation 1 (left of the addition sign). During times of burial, the model only uses the decay portion of equation 1 (right of the addition sign).

Erosion is incorporated by redefining the "surface" as some depth below the top of the bedrock. The model assumes that erosion only takes place during times of burial. The erosion rate range was selected based on trial runs of the model and ice thicknesses were based on reasonable estimates of ice thickness from the local geology. Each sample was stepped through the prescribed exposure scenario (trying all erosion rate and ice thickness combinations) individually, saving the final surface ^{14}C and ^{10}Be concentrations.

We first calculated the accumulation of nuclides under continuous ice cover of various durations (0-50 kyr) for various ice thicknesses (0-50 m) (Figure 3). Fixing erosion rates at 0 mm/yr explores the maximum possible cosmogenic nuclide accumulation under ice cover. Second, we modeled the surface nuclide concentrations that result from 10 kyr-long histories, with various durations of exposure in the early Holocene (5-9 kyr) and burial in the late Holocene (5-1 kyr) for erosion rates of 0-1 mm/yr and did not allow any production through ice. Results indicate that subglacial erosion rates of $\geq$ 0.5 mm/yr are needed to remove an early Holocene exposure signal (Figure 4).

Subglacial Erosion Estimates from Proglacial Lakes

To produce additional estimates of Holocene subglacial erosion rates in the tropics, we used clastic sediment fluxes reported in Rodbell et al. (*8*). That study cored three lakes downvalley from current glaciers in the tropical Andes and used radiocarbon dating to create age-depth profiles for each core. After removing organics, they reported clastic sediment flux as a function of time from the Late Glacial to present.

To translate these clastic sediment flux values into erosion rates, we made several assumptions. First, we made the conservative assumption that all clastic sediment transported to the lake was derived from erosion under the ice and not anywhere else in the catchment. This assumption likely overestimates the erosion rate because erosion was almost certainly occurring by other processes simultaneously. We then accounted for the relative areas of the glacier and lake by measuring them in Google Earth Pro and taking a ratio of their sizes. In doing so, we correct the flux for the lake-glacier size disparity and implicitly assume that glaciogenic sediment input is distributed evenly throughout the lake. For example, if a glacier is twice the size of its lake downvalley, the reported clastic sediment flux is reduced by half to account for the size disparity when translating to subglacial erosion rate. We also used the modern glacial extent in this estimate, which probably causes an overestimate of erosion rate since the glacier was likely larger in the past. For instance, if the glacier were twice as large in the past, then the erosion rate needed to produce the same amount of sediment as the smaller glacier would be half as high.

We used the following formula to calculate erosion rates:

$$E = \frac{A_L}{A_G} * \bar{F_S} * \frac{1}{\rho} * 10$$

where E is erosion rate in mm/yr, A_L is area of the lake in km^2, A_G is area of the glacier in km^2, $\bar{F_S}$ is average sediment flux in g/cm^2/yr through time, and ρ is the density of rock. We considered average sediment fluxes over the past 5 kyr, in addition to the entire Holocene, because Rodbell et al. (2008) infers an increase in glacial activity during the Late Holocene;

this time interval therefore produces a maximum erosion rate estimate. Calculated erosion rates range from ~0.01-0.1 mm/yr (Table S5), which our modeling outlined above (Figure 4) indicates would be insufficient to remove nuclides from early Holocene exposure.

Supplementary Text

Single Cosmogenic Nuclide Dating

Cosmogenic nuclide dating has provided one of the most precise chronometers of past glacial fluctuations (*41*). Single nuclide exposure dating uses the in situ accumulation of cosmogenic nuclides in certain minerals (most commonly ^{10}Be in quartz) during exposure to cosmic radiation as a proxy for exposure age (*41*). This age is therefore calculated by dividing the nuclide concentration by its production rate. Because the production of these nuclides attenuates to nearly zero within the top ~3 m of rock during exposure (~3.5% and 0.9% of surface production rate for ^{14}C and ^{10}Be respectively; Figure S2), considerable erosion during glaciations can remove the preexisting nuclide inventory, restarting the exposure clock.

Two assumptions are made when employing a single nuclide exposure-dating technique: (1) rock surfaces lack inherited cosmogenic nuclides when first exposed, and (2) the samples have remained uncovered, uneroded and in their original configuration since initial exposure. Alternatively, if erosion rates are independently known, eroded samples can be dated (*42*).

To calculate an exposure age from a single nuclide, the concentration of cosmogenic nuclides must be measured and the production rates of the nuclides must be known; however, cosmogenic nuclide production rates vary by latitude and elevation. Earth's atmosphere shields the surface from cosmic radiation, so higher production rates are found at higher elevations. Latitude affects production rates because it is proportional to the average angle with which radiation interacts with Earth's magnetic field and provides varying degrees of shielding (*42*). These spatial variations can be accounted for with scaling models that estimate how production rates vary with atmospheric and geomagnetic shielding (e.g., *40*).

To determine the absolute rate at which nuclides are produced, cosmogenic isotope concentrations have been measured in samples of known age from numerous carefully chosen sites around the world. The variance in the resulting estimates suggests production rate uncertainties for ^{10}Be and ^{14}C of 8.3 and 7.3% respectively (*27*, *43*).

^{14}C-^{10}Be Paired Chronometer

While determining an exposure age from a single cosmogenic nuclide requires knowledge of erosion rates and a simple exposure history, pairing two nuclides with different half-lives can circumvent these limitations. In this case, nuclides preserved through multiple episodes of exposure and burial are measured to discern information about sample exposure *and* burial duration. This insight is possible due to differential decay of the nuclides during ice cover. Owing to improvements in ^{14}C extraction, scientists now pair

^{14}C ($t_{1/2} = 5{,}734$ years) and ^{10}Be ($t_{1/2} = 1.4$ Myr) (*36*, *44*). This system is well suited to reconstruct Holocene glacier variations due to ^{14}C's millennial-scale half-life, and it can be applied to any quartz-bearing bedrock (*45*).

This paired chronometer can be understood by imagining the following nuclide accumulation and decay scenario. When bedrock is first exposed following the last deglaciation, it has been deeply eroded and no longer contains inherited cosmogenic nuclides. At the time of exposure, the bedrock begins to accumulate ^{10}Be and ^{14}C at known rates. If at some point there is a glacier readvance and the bedrock is buried, ^{10}Be concentrations remain constant over Holocene timescales while ^{14}C concentrations decay in proportion to the duration of ice cover. As a result, ^{10}Be concentrations record cumulative exposure, while the ratio of $^{14}C/^{10}Be$ records burial (Figure S1). It should be noted, however, that these nuclides can accumulate and decay over multiple cycles of exposure and burial, which means that similar combinations of ^{14}C and ^{10}Be concentrations may be reached by different histories. These measurements, therefore, are not indicative of a unique exposure-burial history; rather, they help to constrain which histories are and are not possible.

An additional complication is that subglacial erosion during periods of burial reduces the concentration of both nuclides. However, if multiple samples are collected that underwent the same exposure-burial history, the samples will plot along an isochron, with the distance from the origin proportional to erosion depth (Figure S1). Samples are typically taken from

local high points to minimize the chance of local shielding from past sediment cover or deep erosion removing all nuclides.

A final complication is that nuclide production does not cease completely under ice cover. The proportion of nuclides produced under ice cover is typically negligible when there has been extended prior exposure (i.e., > 1 kyr). However, during exposure-burial histories dominated by burial, or in the case of this study, histories with no exposure at all, these concentrations make up a more significant portion of the measurement. During nuclide production at depth, ^{14}C accumulates at a higher proportion of its surface production than ^{10}Be (Figure S2), leading to an elevated $^{14}C/^{10}Be$ ratio, a key indicator that the nuclide inventory has been produced in this fashion (Figure S1).

Modern Andean Climate

Whether a glacier is located in the tropics, mid, or high latitudes tends to control the distribution of accumulation and ablation throughout the year (*46*). Because annual temperature swings are small near the equator, ablation occurs year-round in the tropics and nearly so in the outer tropics. The primary difference between the inner and outer tropics is in their accumulation periods, which is related to the north-south migration of the Intertropical Convergence Zone (ITCZ). The ITCZ is located where the Northern and Southern Hemisphere trade winds meet, roughly around the equator. The solar heating in the region causes air to rise, creating a consistent band of clouds and precipitation. The location of the ITCZ at any given time is a function of the sun's zenith position. As a result,

the ITCZ migrates north of the equator during the boreal summer, and south of the equator during winter, driving precipitation variations with its movement (Figure 1A). Due to this migration, the outer tropics receive accumulation just once per year, while the inner tropics receive accumulation twice per year.

Mean annual precipitation in the South American tropics is also influenced by teleconnections related to El Niño-Southern Oscillation. El Niño years are correlated with below normal rainfall over tropical South America and warmer than average conditions over tropical and subtropical South America while La Niña years bring the opposite trends (*47*). During El Niño years, eastern Pacific sea surface temperatures are warmer than normal, which increases convection on the west coast of South America. Precipitation is normally delivered to the tropical Andes by the tropospheric easterlies, but this pattern is obstructed by the increased coastal convection, reducing overall precipitation during El Niño years. The full range of factors that influence precipitation remains unknown as ENSO only explains 15% of tropical precipitation variability (*48*).

Finally, the South American Summer Monsoon brings precipitation to the southern tropical Andes during the austral summer. Like all monsoons, this precipitation is driven by a temperature gradient between land and ocean. In this case, the land in the tropics is warmer than the ocean, which drives moist air to flow towards the continent. The topography of the region then funnels precipitation to the Andes (*49*). Therefore, stronger temperature gradients channel more precipitation.

Site Descriptions

Cocuy Glacier, Colombia. This is a small 1.56 km^2 glacier located in the Sierra Nevada del Cocuy in northeastern Colombia (6.4°N, 72.3°W, 5123 m, Figure S3). Three samples were taken here by Gordon Bromley (University of Maine) between 2012 and 2018. Model studies show that glaciers in this region are particularly sensitive to changes in temperature as opposed to changes in precipitation(*50*). During the last 50 years, Colombian glaciers lost 50% of their area, and analyses show that temperature has increased by greater than 1°C over the same period (*24*).

Only one study has investigated Cocuy Glacier's Holocene extent history. Van Der Hammen et al. (*51*) presents a radiocarbon age of 12.32 ± 0.1 ^{14}C ka B.P. from organic material in lake varves immediately behind the Late Glacial moraine at Cocuy Glacier. The workers also note only one set of moraines further upvalley, which they interpret to be Neoglacial in age, forming within the past 0.5 kyr. In arriving at this interpretation, they point to the similar sediment thickness in the lake behind this moraine and several moraine-dammed lakes from the Sierra Nevada de Santa Marta (~200 km northeast), which have basal radiocarbon ages of ~0.3 ka.

Holocene pollen and glaciogenic sediment records from four lakes in the Cordillera de Merida (~275 km northeast of Cocuy Glacier) provide a detailed history of vegetation and glacier changes in the region from 15 ka to present. The pollen record indicates the highest elevations were unvegetated until about 11 ka, consistent with extensive ice before the Holocene (*15*). Between 12.6 and 9.5 ka, the influx of glacial sediments to many lakes

declined, and ceased completely in locations that are presently unglaciated. From 4 ka until the LIA, the pollen record indicates a cooling trend while glaciogenic sediment fluxes to lakes with headwalls above 4,600 m increased, consistent with growing glacier sizes during this period (*15*, *52*). This is in contrast with glaciers located on lower elevation headwalls, whose proglacial lake sediment fluxes remained constant (*52*). These records are consistent with the few data points that exist at Cocuy Glacier, suggesting that following latest Pleistocene glaciation, ice extent was relatively small during the early Holocene but expanded during the late Holocene.

Queshque Glacier, Peru. This is a small, southwestern-facing glacier (2.35 km^2) located in the Cordillera Blanca in western Peru (9.8°S, 77.3°W, 5578 m, Figure S4). Emilio Mateo (Ohio State University) sampled bedrock in six locations near the toe of the modern ice margin in 2019. A combination of aerial imagery and digital elevation data suggests that this glacier site lost 85% of its volume between 1962 and 1999 (*22*, *53*). An accompanying heuristic sensitivity analysis shows that the ~0.25°C/decade temperature increase is sufficient to account for this loss (*22*).

Clastic sediment records from two lakes immediately downvalley from Queshque Glacier offer insight into its past extent fluctuations (*16*). Decreasing glaciogenic sediment fluxes suggest the glacier retreated during the Late Glacial period and between 12 and 8 ka. The glacier then advanced during the mid-Holocene, likely between 8 and 5 ka, reaching a maximum sediment flux 4-5 ka. Finally, these records indicate the glacier may have

remained about the same size, or retreated slightly between 4 ka and the LIA, at which point there was a marked advance (*16*).

Charquini Norte and Zongo Glaciers, Bolivia. Charquini Norte (16.29°S, 68.10°W, 5257 m, Figure S5) and Zongo Glaciers (16.27°S, 68.13°W, 5257 m, Figure S6) are located across a valley from one another in northwestern Bolivia. They are both small alpine glaciers (0.08 and 1.93 km^2 respectively). Eleven total samples from these glaciers were taken by Vincent Jomelli (French National Centre for Scientific Research) in 2019: six samples at Charquini beginning at the ice margin and extending ~0.9 km down valley, and five samples at Zongo along the ice margin. Charquini Norte Glacier and Zongo Glacier have lost approximately 0.35 km^2 and 0.15 km^2 of their surface areas since 1930 (*23*). While weather station records indicate that precipitation in western Bolivia and eastern Peru has decreased slightly, temperatures have increased by more than 1°C over the last century (*23*, *54*). This suggests a larger role for temperature than precipitation in the overall mass balance changes (*23*, *54*). Glacial retreat at both sites started roughly in the 17^{th} century after the region experienced the LIA (*21*, *55*). Over the last two decades of the 20^{th} century, the rate of retreat at Charquini Norte Glacier increased by a factor of four (*55*).

Glaciogenic lake sediment fluxes, radiocarbon dates, and cosmogenic nuclide dates from local valleys shed light on the extent history of these glaciers. Basal radiocarbon ages from lakes in the Zongo and Milluni valleys (~8 km away) range from 9.8 to 11.0 ka (*56*), while cosmogenic nuclide ages of Late Glacial moraines in the Palcoco valley (~20 km away)

range from 8.2-16.2 ka (*57*), suggesting these glaciers were larger than today until the early Holocene. LIA moraines immediately upvalley of these Late Glacial moraines are constrained by minimum-limiting radiocarbon ages of 0.2-0.63 ka (*58*). The lack of other moraines between the Late Glacial and LIA moraines suggests the most extensive Holocene advance in the Palcoco valley occurred during the LIA (*58*, *59*). Farther downvalley, glaciogenic sediment fluxes to Laguna Taypi Chaka Khota are consistent with this moraine record, and suggest that glacial activity increased between 2.5 ka and the LIA (*8*, *58*). Taken together, these data suggest a Holocene history in the Charquini/Zongo region similar to our other study regions; glaciers were generally large until the early Holocene, retreated for a few millennia in the early or mid-Holocene, and finally advanced to a Holocene maximum during the LIA (*8*).

Quelccaya Ice Cap, Peru. The Quelccaya Ice Cap (13.9°S, 70.8°W, 5740 m; Figure S8), Peru is the largest tropical ice mass in the world spanning 40 km^2. Meredith Kelly (Dartmouth College) took five samples along the ice margin in 2003 and 2008. During the period from 1980-2010, this ice cap shrank at a rate of 0.57 ± 0.10 km^2yr^{-1} (*60*). Statistical analyses of data from weather stations indicate that there have been no significant changes in precipitation in this region in the past five decades (*48*, *61*, *62*). On the other hand, temperature at this location has been increasing steadily over at least the past six decades (*63*).

Directly downvalley from our samples, radiocarbon ages indicate that the glacier retreated to its late Holocene extent by around 11.6 ka (*64*). After this, it retreated further, and was

as small as or smaller than today from 7 to 5.2 ka (*9*). This constraint is evidenced by in-place plants that recently thawed from the ice margin and are radiocarbon dated to 5.2 ka. Had the ice been smaller than today at any point since then, the plant remains would have decomposed (*9*). Thus, from 5.2 ka to present, the glacier advanced and was larger than today. This Holocene glacial extent history is mirrored closely by glaciogenic sediment fluxes to Laguna Pacococha on the northwestern side of the QIC (*8*). Finally, ^{10}Be moraine ages from Qori Kalis, an outlet glacier of QIC, indicate maximum late Holocene advances culminated at ~2.7 and ~0.5 ka (*65*).

Supplementary Figures

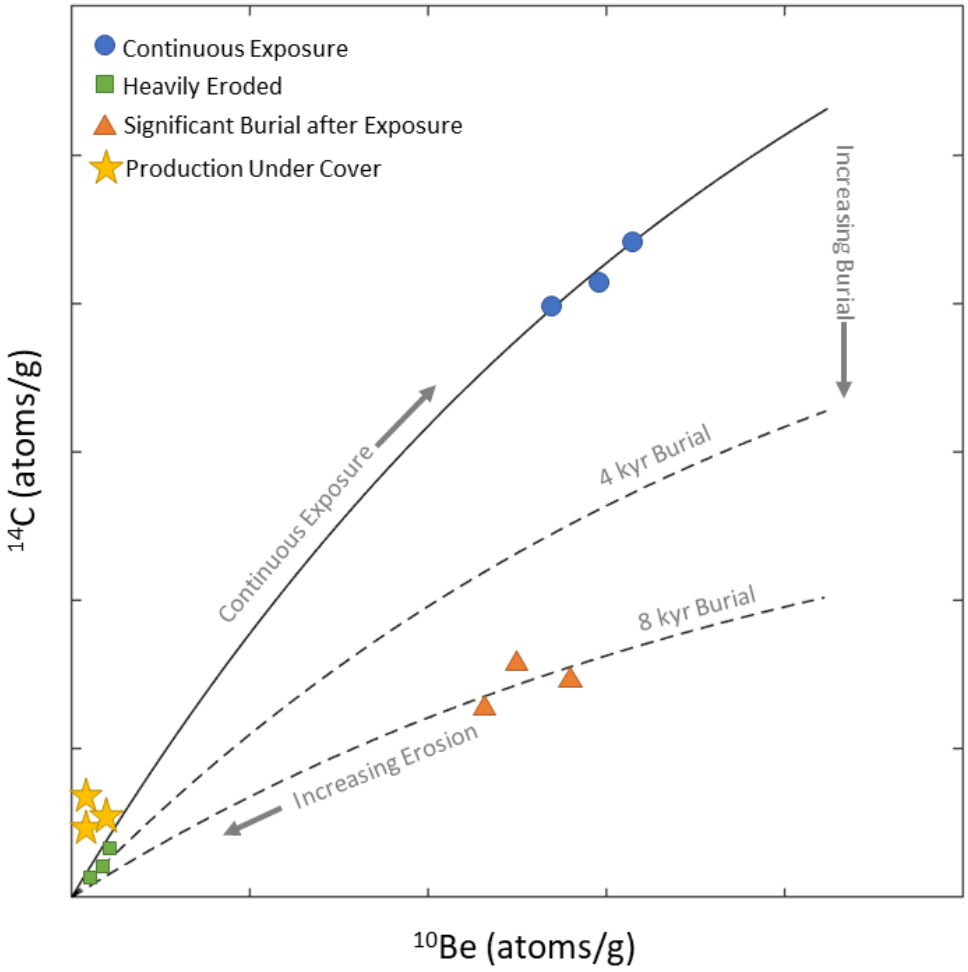

Figure S1: Schematic diagram showing how various exposure-burial histories plot in ^{14}C-^{10}Be space. Most of the low-nuclide samples measured for this study plot near the origin above the continuous exposure curve (stars).

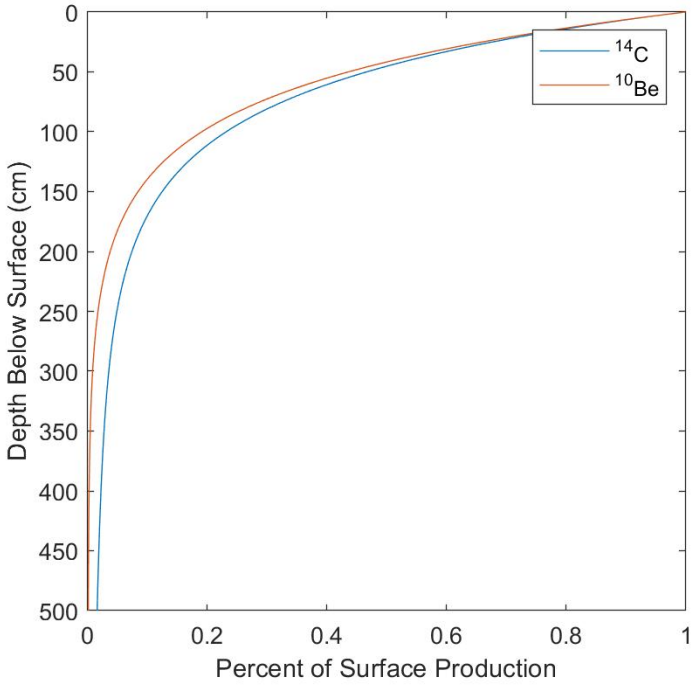

Figure S2: Production rate attenuation with depth in bedrock for both ^{14}C and ^{10}Be in a low-latitude, high-elevation area.

Figure S3: Google Earth Image of Cocuy Glacier and sample locations.

Figure S4: Google Earth images of Queshque Glacier and selected sample site field photos.

Figure S5: Google Earth image of Charquini Norte Glacier and selected sample site field photos.

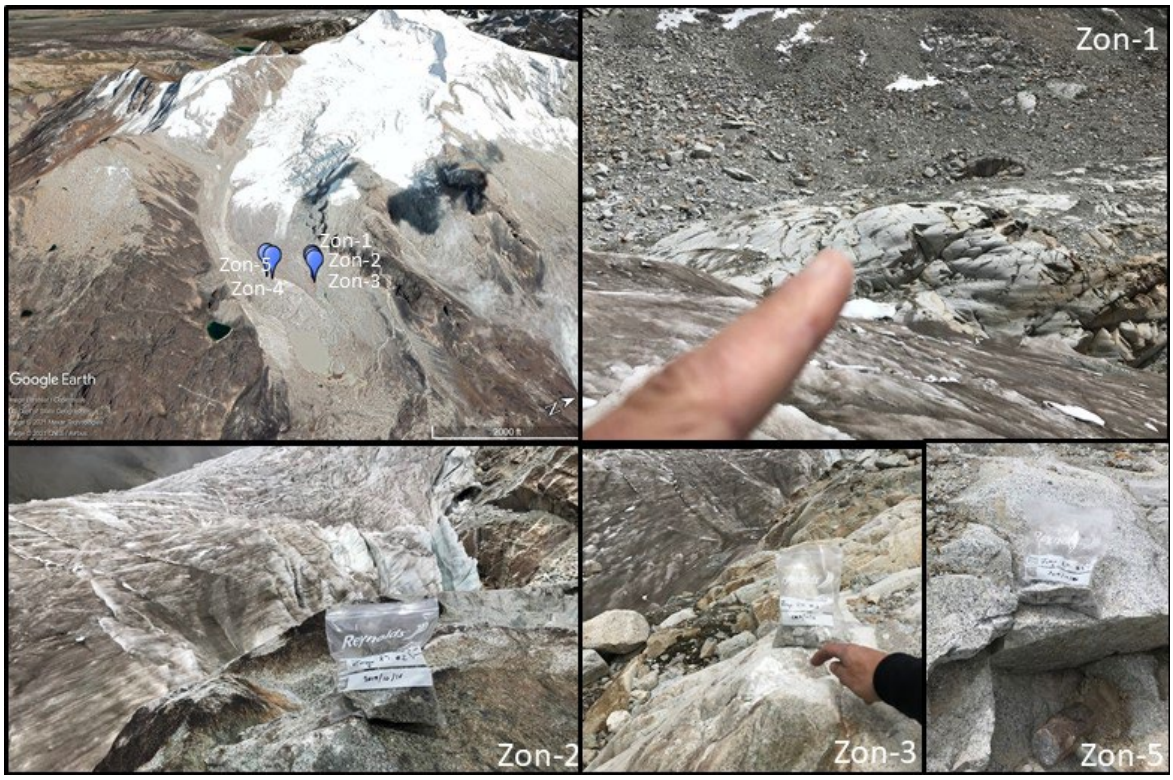

Figure S6: Google Earth image of Zongo Glacier and selected sample site field photos.

Figure S7: Google Earth image of the Quelccaya Ice Cap and selected sample site field photos.

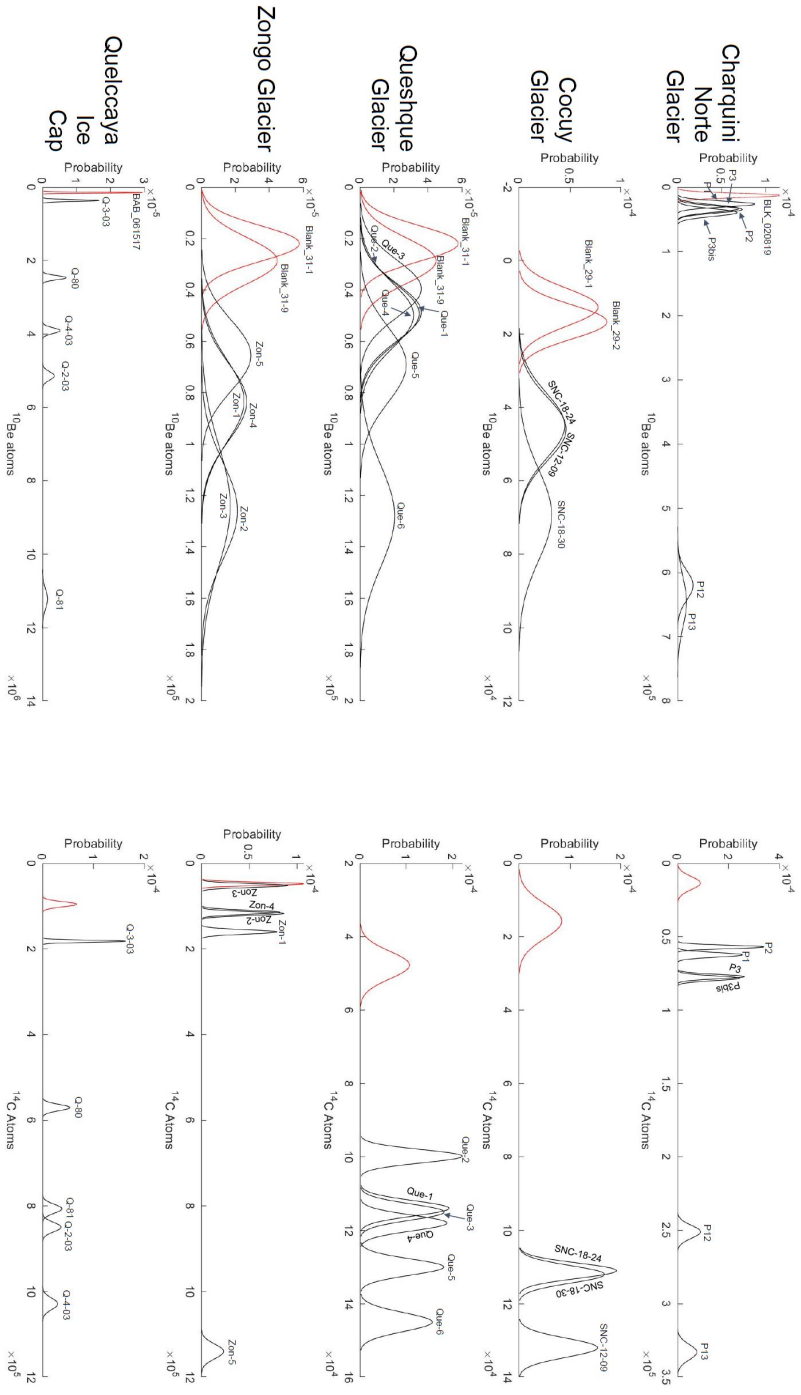

Figure S8: ^{10}Be and ^{14}C nuclide abundances measured for each sample (black) compared to laboratory process blanks (red). Each row represents a given glacier.

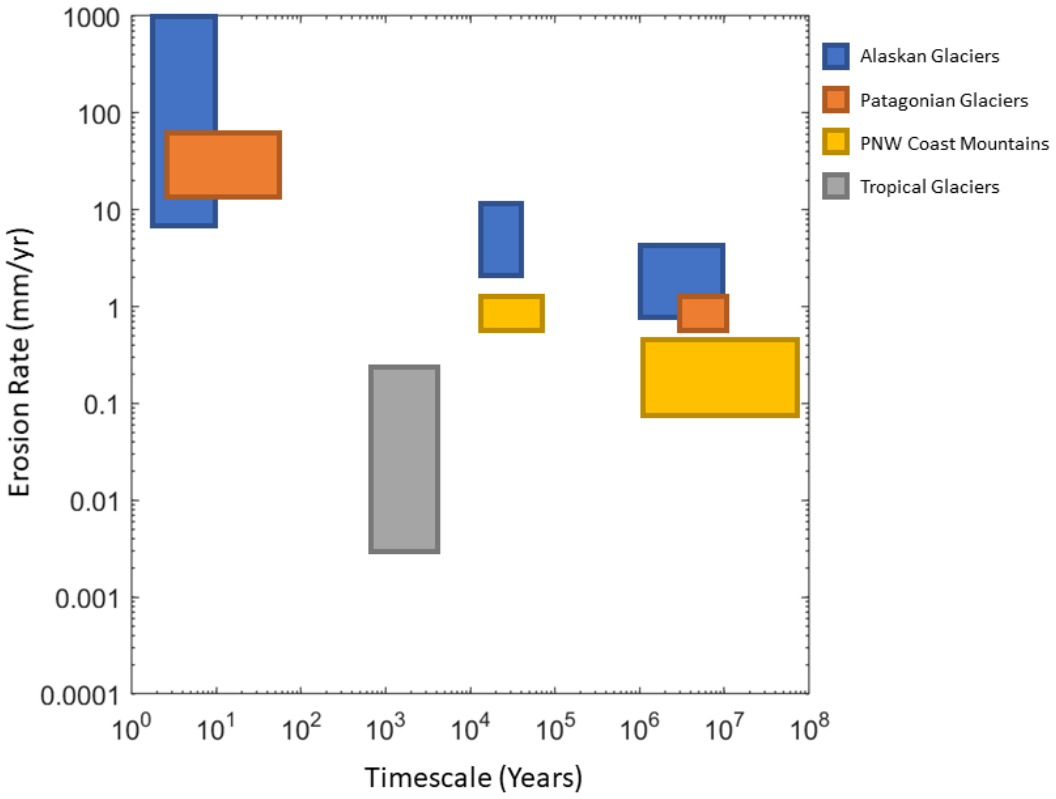

Figure S9: Synthesis of global erosion rates adapted from Koppes et al. (66). Estimates from tropical glaciers are from Vickers et al. (11), Jomelli et al. (21) and calculations based on Rodbell et al. (8) lake sediment flux estimates.

Supplementary Tables

Table S1: ^{10}Be and ^{14}C sample data. All uncertainties are 1σ.

Sample	Latitude (DD)	Longitude (DD)	Elevation (m asl)	Thickness (cm)	Shielding	^{10}Be (10^3 atoms/g)	^{14}C (10^4 atoms/g)	^{10}Be age[1] (yr)	^{14}C age[1] (yr)	Collection Year
Cocuy Glacier										
SNC-12-09	-6.36569	-72.30404	4723	2.3	0.979	1.56±0.43	2.33±0.11	37±10	204±14	2012
SNC-18-24	-6.37353	-72.30497	4838	1.5	0.98	2.72±0.62	1.88±0.10	61±14	153±8	2018
SNC-18-30	-6.37316	-72.30504	4840	1.5	0.985	1.51±0.43	2.19±0.12	34±10	179±13	2018
Quelccaya Ice Cap										
Q-2-03	-13.9299	-70.8531	5225	3.0	0.969	25.62±0.57	21.60±0.78	5656±52	1959±80	2003
Q-3-03	-13.93	-70.8526	5210	5.0	0.995	1.80±0.12	2.01±0.71	386±26	152±54	2003
Q-4-03	-13.9298	-70.853	5220	4.0	0.995	21.69±0.43	26.20±0.84	4868±92	2464±92	2003
Q-80	-13.9327	-70.8537	5196	3.0	0.996	12.08±0.28	13.40±0.76	2824±65	1113±68	2008
Q-81	-13.9332	-70.8567	5225	3.0	0.997	56.00±1.34	19.80±0.79	10970±263	1720±76	2008
Queshque Glacier										
Que-1	-9.79249	-77.25158	4710	2.75	0.96	0.69±0.33	1.33±0.09	18±10	124±10	2019
Que-2	-9.792516	-77.25153	4714	3	0.96	0.64±0.30	1.05±0.08	16±10	98±9	2019
Que-3	-9.792832	-77.25150	4714	2	0.96	0.35±0.27	1.37±0.09	9±7	127±10	2019
Que-4	-9.793069	-77.25262	4707	2	0.94	1.7±0.60	1.42±0.09	31±19	135±11	2019
Que-5	-9.794099	-77.25394	4692	2.75	0.93	1.2±0.40	1.64±0.09	32±12	160±12	2019
Que-6	-9.794391	-77.25555	4701	2.5	0.92	3.0±0.58	1.94±0.09	83±18	191±13	2019
Charquini Glacier										
P1	-16.29507	-68.10237	5130	2.9	0.97	2.4±1.0	2.4±0.23	52±22	191±21	2018

Sample	Latitude (DD)	Longitude (DD)	Elevation (m asl)	Thickness (cm)	Shielding	^{10}Be (10^3 atoms/g)	^{14}C (10^4 atoms/g)	^{10}Be age[1] (yr)	^{14}C age[1] (yr)	Collection Year
P2	-16.29386	-68.10281	5131	3.3	0.97	3.2±0.93	2.19±0.23	69±24	174±21	2018
P3	-16.29256	-68.10301	5099	4.8	0.97	3.7±1.2	3.12±0.23	82±30	258±23	2018
P12	-16.28814	-68.10618	5099	3.1	0.97	4.7±1.2	3.09±0.23	103±24	252±23	2018
P13	-16.28835	-68.10615	4911	3.7	0.97	97.6±3.7	8.78±0.23	2577±180	819±49	2018
PBIS	-16.29206	-68.10293	4915	4.3	0.97	120±7.4	12.0±0.26	3197±272	1125±66	2018
Zongo Glacier										
Zon-1	-16.28062	-68.13677	4978	2.0	0.98	2.4±0.37	3.26±0.10	30±10	275±17	2019
Zon-2	-16.28044	-68.13659	4975	3.5	0.98	2.8±0.54	2.28±0.10	66±14	192±13	2019
Zon-3	-16.27877	-68.13613	4971	1.7	0.98	2.9±0.69	1.02±0.09	66±17	84±8	2019
Zon-4	-16.27875	-68.13631	5005	2.0	0.99	1.9±0.50	2.37±0.09	42±13	193±12	2019
Zon-5	-16.27875	-68.13642	5012	3	0.99	1.3±0.44	22.80±0.34	28±11	2199±131	2019

[1] Calculated using the CRONUS-Earth online calculator v.3 with the LSDn scaling scheme (*39*, *40*).

Table S2: ^{10}Be sample processing details.

Sample	Be Carrier Added (g)	^{10}Be/^{9}Be (10^{-13})	Quartz Mass (g)	^{10}Be Blank
Cocuy Glacier				
SNC-12-09	0.7775	0.04±0.006	20.0319	29-1, 29-2
SNC-18-24	0.7737	0.05±0.009	20.0862	29-1, 29-2
SNC-18-30	0.7727	0.03±0.007	20.0661	29-1, 29-2
Quelccaya Ice Cap				
Q-2-03	0.2601	2.92±0.05	20.0666	BAB_061517

Sample	Be Carrier Added (g)	$^{10}Be/^{9}Be$ (10^{-13})	Quartz Mass (g)	^{10}Be Blank
Q-3-03	0.2601	0.28±0.01	20.0336	BAB_061517
Q-4-03	0.2601	2.24±0.04	18.0134	BAB_061517
Q-80	0.2601	1.44±0.03	20.3979	BAB_061517
Q-81	0.2607	6.27±0.13	20.0366	BAB_061517
Queshque Glacier				
Que-1	0.6735	0.04±0.01	0.6735	31-1, 31-9
Que-2	0.7017	0.04±0.009	0.7017	31-1, 31-9
Que-3	0.6965	2.03±0.009	0.6965	31-1, 31-9
Que-4	0.7034	1.04±0.011	0.7034	31-1, 31-9
Que-5	0.6362	6.06±0.013	0.6362	31-1, 31-9
Que-6	0.6852	2.11±0.016	0.6852	31-1, 31-9
Charquini Norte Glacier				
P1	0.281	0.01±0.002	5.5163	BLK_020819
P2	0.2906	0.02±0.003	6.8786	BLK_020819
P3	0.2828	0.02±0.003	5.4985	BLK_020819
P3bis	0.2872	0.02±0.003	5.6438	BLK_020819
P12	0.2872	0.3±0.011	6.2222	BLK_020819
P13	0.2857	0.3±0.019	5.2822	BLK_020819
Zongo Glacier				
Zon-1	0.7012	0.07±0.013	42.5175	31-1, 31-9
Zon-2	0.7195	0.1±0.015	34.9665	31-1, 31-9
Zon-3	0.7148	0.1±0.019	33.8695	31-1, 31-9
Zon-4	0.6809	0.07±0.013	30.2193	31-1, 31-9
Zon-5	0.7095	0.5±0.011	31.0091	31-1, 31-9

Supplementary Table S3: ^{14}C sample processing details. All uncertainties are 1σ.

Sample	Quartz Mass (g)	C Yield (µg)	Diluted C Mass (µg)	$^{14}C/C$ (10^{-14})	^{14}C (atoms/g) (10^4)	Effective Blank (atoms) (10^4)
Cocuy Glacier						
SNC-12-09	5.0272	26.2	112.4	2.36±0.03	2.32±0.11	1.57±0.445
SNC-18-24	5.1179	32.3	99.3	2.25±0.03	1.86±0.10	1.57±0.445
SNC-18-30	4.4437	18.6	112.6	2.00±0.03	2.17±0.12	1.57±0.445
Quelccaya Ice Cap						
Q-2-03	3.4872	5.5	104.5±1.3	16.41±0.01	21.9±0.40	9.533±0.59
Q-3-03	3.7742	5.0	111.3±1.4	3.437±0.00	2.56±0.20	9.533±0.59
Q-4-03	3.5279	9.1	111.1	18.65±0.01	26.71±0.40	9.533±0.59
Q-80	3.4983	6.3	107.3	10.79±0.00	13.9±0.30	9.533±0.59
Q-81	3.5603	5.3	108.4	15.03±0.00	20.3±0.3	9.533±0.59
Queshque Glacier						
Que-1	5.004	4.2	92.6	2.48±0.03	1.33±0.09	4.77±0.374
Que-2	4.9398	3.5	111.3	1.79±0.02	1.05±0.08	4.77±0.374
Que-3	4.8881	4	102.6	2.24±0.03	1.37±0.09	4.77±0.374
Que-4	4.9383	3.8	112.2	2.10±0.03	1.42±0.09	4.77±0.374
Que-5	5.0353	3.5	100.4	2.60±0.03	1.64±0.09	4.77±0.374
Que-6	5.0219	4	112	2.60±0.03	1.94±0.09	4.77±0.374
Charquini Norte Glacier						
P1	2.036	3.5	111.7	1.11	2.40±0.23	1.34±0.445
P2	1.9909	2.9	115.8	97.9	2.19±0.23	1.34±0.445
P3	2.0402	3.4	109.8	1.40	3.12±0.23	1.34±0.445

Sample	Quartz Mass (g)	C Yield (µg)	Diluted C Mass (µg)	$^{14}C/C$ (10^{-14})	^{14}C (atoms/g) (10^4)	Effective Blank (atoms) (10^4)
P3bis	2.0998	3.7	92.6	1.68	3.09±0.23	1.34±0.445
P12	2.707	2.6	95.3	5.25	8.78±0.23	1.34±0.445
P13	2.6746	3.6	113.3	5.87	1.20±0.26	1.34±0.445
Zongo Glacier						
Zon-1	4.8993	6.8	92	4.52	3.26	4.77±0.374
Zon-2	4.9913	9.4	113.3	2.86	2.28	4.77±0.374
Zon-3	5.021	10.4	113.1	1.76	1.03	4.77±0.374
Zon-4	4.9289	9.8	112.8	2.92	2.37	4.77±0.374
Zon-5	4.9992	5.7	113.4	21.0	22.8	4.77±0.374

Table S4: ^{10}Be Blank Data. Uncertainties are 1σ.

Blank ID	Be carrier (g)	$^{10}Be/^{9}Be$ (10^{-15})	^{10}Be (10^4 atoms)
BAB_061517	0.2585	8.10±0.76	14.56±1.36
BLK_020819	0.2885	0.62±0.17	1.28
Blank_29-1	0.7648	0.99±0.40	1.27
Blank_29-2	0.7698	1.29±0.36	1.67
Blank_31-1	0.7737	1.68±0.53	2.19
Blank_31-9	0.6913	2.46±0.77	0.89

Table S5: Calculation data for erosion rate estimates from proglacial lake sediment fluxes reported in Rodbell et al. (*8*).

Lake Name	**Latitude**	**Longitude**	**Lake Area (km^2)**	**Glacier Area (km^2)**	**Average Flux (past 10 kyr g/cm/yr)**	**Average Flux (past 5 kyr; g/cm/yr)**	**Rock Density (g/cm^3)**	**Inferred Erosion Rate (past 10 kyr mm/yr)**	**Inferred Erosion Rate (past 5 kyr; mm/yr)**
Queshque	9.82 °S	77.3 °W	0.10	2.35	0.09	0.15	2.67	0.013	0.024
Pacococha	13.95 °S	70.88 °W	0.11	1.66	0.02	0.03	2.67	0.005	0.009
Huarmicocha	10.43 °S	76.84 °W	0.06	0.028	0.01	0.01	2.67	0.067	0.08